

## Long-Distance Coherent Propagation of High-Velocity Antiferromagnetic Spin Waves

Hanchen Wang<sup>1,2,3,\*</sup>, Rundong Yuan<sup>1,\*</sup>, Yongjian Zhou,<sup>4,\*</sup> Yuelin Zhang,<sup>1</sup> Jilei Chen,<sup>5,2</sup> Song Liu,<sup>2,5</sup> Hao Jia,<sup>2,5</sup> Dapeng Yu,<sup>2,5</sup> Jean-Philippe Ansermet<sup>6,5,†</sup>, Cheng Song,<sup>4,‡</sup> and Haiming Yu<sup>1,2,§</sup>

<sup>1</sup>Fert Beijing Institute, MITT Key Laboratory of Spintronics, School of Integrated Circuit Science and Engineering, Beihang University, Beijing 100191, China

<sup>2</sup>International Quantum Academy, Shenzhen 518048, China

<sup>3</sup>Department of Materials, ETH Zurich, Zurich 8093, Switzerland

<sup>4</sup>Key Laboratory of Advanced Materials (MOE), School of Materials Science and Engineering, Tsinghua University, Beijing 100084, China

<sup>5</sup>Shenzhen Institute for Quantum Science and Engineering, Southern University of Science and Technology, Shenzhen 518055, China

<sup>6</sup>Institute of Physics, Ecole Polytechnique Fédérale de Lausanne (EPFL), 1015, Lausanne, Switzerland



(Received 22 November 2022; revised 6 January 2023; accepted 10 February 2023; published 28 February 2023)

We report on coherent propagation of antiferromagnetic (AFM) spin waves over a long distance ( $\sim 10$   $\mu\text{m}$ ) at room temperature in a canted AFM  $\alpha\text{-Fe}_2\text{O}_3$  owing to the Dzyaloshinskii-Moriya interaction (DMI). Unprecedented high group velocities (up to 22.5 km/s) are characterized by microwave transmission using all-electrical spin wave spectroscopy. We derive analytically AFM spin-wave dispersion in the presence of the DMI which accounts for our experimental results. The AFM spin waves excited by nanometric coplanar waveguides have large wave vectors in the exchange regime and follow a quasilinear dispersion relation. Fitting of experimental data with our theoretical model yields an AFM exchange stiffness length of 1.7  $\text{\AA}$ . Our results provide key insights on AFM spin dynamics and demonstrate high-speed functionality for AFM magnonics.

DOI: [10.1103/PhysRevLett.130.096701](https://doi.org/10.1103/PhysRevLett.130.096701)

Spin waves or magnons [1–4] as collective spin excitations can transport coherent spin information in a magnetic media over long distances [5–7] without suffering from Ohmic loss, and are therefore promising for magnon-based computing with low-power consumption [8,9]. So far, an overwhelming majority of magnonic research has been conducted in ferromagnetic or ferrimagnetic materials, such as yttrium iron garnet (YIG) [10–14], permalloy [15–18], and magnetic multilayers [19–21]. In ferromagnetic (FM) materials, long wavelength spin waves are predominantly affected by dipolar interactions, resulting in Damon-Eshbach (DE) and backward-volume (BV) modes with distinct configurations of the magnetization ( $\mathbf{m}$ ) and wave vector ( $\mathbf{k}$ ) and with nondegenerate dispersions [Fig. 1(a)]. This anisotropy hinders spin waves from propagating through a curved circuit [22] and leads to vulnerability to external field disturbances. Thus, it is desirable to excite high- $k$  exchange spin waves in ferromagnets with short wavelengths that are substantially less anisotropic. Exchange spin waves in ferromagnets [23] follow a parabolic dispersion relation, suggesting an increasing group velocity for higher  $k$ . So far, it has been extremely challenging to excite exchange spin waves with a velocity around 1 km/s and a wavelength below 100 nm [6,24,25]. In antiferromagnetic (AFM) materials, these challenges and obstacles are inherently neutralized because spin waves are insensitive to disturbing magnetic fields [26]

and can propagate with higher velocities [27]. However, new challenges arise as antiferromagnets have zero net moment [28]. In addition, antiferromagnetic spin waves fall typically in the THz or sub-THz frequency regime [29,30] and are so far mostly excited using an optical method [27,31] that is difficult to integrate with on-chip magnonic devices. Diffusive transport of multichromatic magnons has been studied by electrical injection and detection using Platinum contacts [7,32–36] which are insensitive to phase coherency. All-electrical excitation and detection of coherent AFM spin waves [37] are highly desired for magnonics, but remain challenging. Recently, advanced microwave technology based on solid-state extenders enabled frequency multiplication of a conventional GHz source into sub-THz generators for all-electrical AFM magnon excitation [38,39]. Until now, coherent AFM spin waves have been electrically excited only with  $k = 0$ , i.e., antiferromagnetic resonance (AFMR) [31,38–40] [e.g., black arrow in Fig. 1(b)], which has zero group velocity in a canted AFM [41]. High-velocity propagating AFM exchange spin waves with electrical excitation has not been realized so far.

In this Letter, we experimentally demonstrate coherent propagation of AFM exchange spin waves over a long distance (10  $\mu\text{m}$ ) in  $\alpha\text{-Fe}_2\text{O}_3$  with a high group velocity (22.5 km/s) at room temperature. The velocity is approximately 1 order of magnitude higher than that of FM exchange spin waves [6,24,25].  $\alpha\text{-Fe}_2\text{O}_3$  also known as

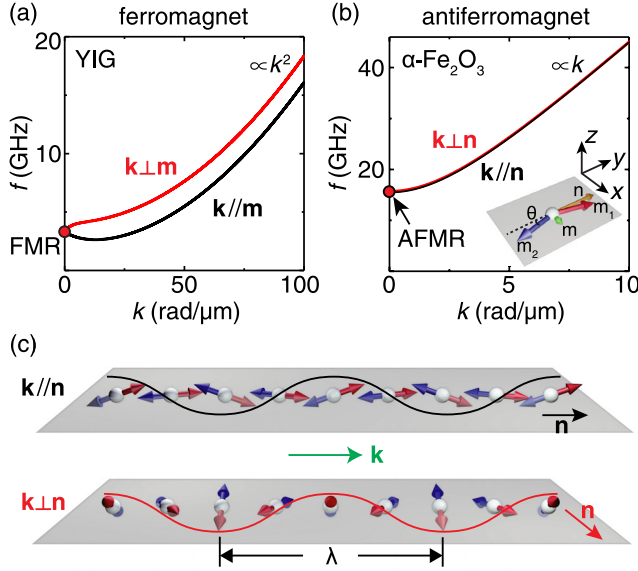


FIG. 1. (a) Ferromagnetic-type spin-wave dispersion for a 200 nm-thick YIG film. The  $\mathbf{k} \perp \mathbf{m}$  and  $\mathbf{k} \parallel \mathbf{m}$  modes are separated due to the dipolar interaction. The  $k = 0$  mode is the ferromagnetic resonance (FMR). Exchange-dominated spin waves follow a quadratic  $k^2$  relation. (b) Spin-wave dispersion of a canted antiferromagnet  $\alpha\text{-Fe}_2\text{O}_3$ . The  $\mathbf{k} \perp \mathbf{n}$  and  $\mathbf{k} \parallel \mathbf{n}$  modes as illustrated in (c) are degenerate and adhere to a linear  $k$  dependence in the exchange regime. The black arrow marks the AFMR with  $k = 0$ . Inset: canting of two sublattices induced by the DMI. (c) Illustrations of exchange spin waves in an easy-plane antiferromagnet at two different configurations, namely, wave vector  $\mathbf{k}$  parallel and perpendicular to Néel vector  $\mathbf{n}$ .

hematite is an insulating antiferromagnet [42–48] with ultralow magnetic damping ( $\sim 10^{-5}$ ) [32] and high Néel temperature ( $\sim 960$  K) [49]. At room temperature (above its Morin temperature  $T_M \simeq 260$  K),  $\alpha\text{-Fe}_2\text{O}_3$  is in an easy-plane antiferromagnetic phase, where its Néel vector  $\mathbf{n}$  lies in the plane [Fig. 1(c)] normal to the corundum crystal  $c$  axis [50]. The bulk Dzyaloshinskii-Moriya interaction

(DMI) in  $\alpha\text{-Fe}_2\text{O}_3$  induces a small canted moment [51] as shown in the inset of Fig. 1(b). The weak canted moment ( $\sim 1.2$  emu/cm<sup>3</sup>) existing in the easy plane is characterized by x-ray diffraction and vibrating sample magnetometer as shown in the Supplemental Material, Fig. S1 [52]. Although the canted moment is negligibly weak as a net magnetic moment ( $\sim 1\%$  of YIG magnetic moment), it facilitates AFMR excitation with conventional microwave antennas [50,51]. As the easy-plane anisotropy is remarkably small ( $H_a \sim 0.06$  mT), the AFMR frequency drops to around 20 GHz, which is accessible using conventional microwave techniques. The negligible easy-plane anisotropy also allows the Néel vector  $\mathbf{n}$  to rotate freely in plane with respect to the spin-wave wave vector  $\mathbf{k}$ , as illustrated in Fig. 1(c) for  $\mathbf{k} \parallel \mathbf{n}$  and  $\mathbf{k} \perp \mathbf{n}$  as examples. Unlike in ferromagnets where  $\mathbf{k} \perp \mathbf{m}$  (DE) and  $\mathbf{k} \parallel \mathbf{m}$  (BV) behave differently [Fig. 1(b)], spin waves in antiferromagnets are degenerate for  $\mathbf{k} \perp \mathbf{n}$  and  $\mathbf{k} \parallel \mathbf{n}$  [Fig. 1(c)] and any intermediate angle because the AFM spin-wave dispersion is not affected by dipolar interaction but fully determined by exchange interaction. Recently, Boventer *et al.* [51] have theoretically derived the AFMR ( $k = 0$ ) formula for  $\alpha\text{-Fe}_2\text{O}_3$ . However, literature on the spin-wave dispersion for an easy-plane antiferromagnet with DMI remains elusive.

Let us first derive and discuss the spin-wave dispersion for an antiferromagnet with DMI-induced canting and easy-plane anisotropy like that of  $\alpha\text{-Fe}_2\text{O}_3$  [Fig. 1(b)]. We consider a one-dimensional spin chain with two sublattices  $\mathbf{m}_1$  and  $\mathbf{m}_2$  that are antiferromagnetically coupled and confined in the easy plane. In the AFM system, the exchange energy, Zeeman energy, anisotropy energy, and Dzyaloshinskii-Moriya (DM) energy constitute the total free energy, from which we obtain the equations of motion describing the dynamics of two spin sublattices in a mean-field approximation (see Sec. II in the Supplemental Material [52]),

$$\begin{cases} \frac{d\mathbf{m}_1}{dt} = -\gamma\mu_0\mathbf{m}_1 \times [\mathbf{H}_0 - H_{\text{ex}}\mathbf{m}_2 - \frac{1}{2}H_{\text{ex}}a_{\text{ex}}^2\nabla^2\mathbf{m}_2 - H_A(\mathbf{m}_1 \cdot \hat{\mathbf{z}})\hat{\mathbf{z}} + H_a(\mathbf{m}_1 \cdot \hat{\mathbf{y}})\hat{\mathbf{y}} + H_{\text{DM}}(\mathbf{m}_2 \times \hat{\mathbf{z}})] \\ \frac{d\mathbf{m}_2}{dt} = -\gamma\mu_0\mathbf{m}_2 \times [\mathbf{H}_0 - H_{\text{ex}}\mathbf{m}_1 - \frac{1}{2}H_{\text{ex}}a_{\text{ex}}^2\nabla^2\mathbf{m}_1 - H_A(\mathbf{m}_2 \cdot \hat{\mathbf{z}})\hat{\mathbf{z}} + H_a(\mathbf{m}_2 \cdot \hat{\mathbf{y}})\hat{\mathbf{y}} - H_{\text{DM}}(\mathbf{m}_1 \times \hat{\mathbf{z}})], \end{cases} \quad (1)$$

where  $\mathbf{H}_0$  is the external magnetic field,  $H_{\text{ex}}$  is the strength of the exchange field,  $a_{\text{ex}}$  is the exchange stiffness length (see the Supplemental Material, Sec. II [52]),  $H_A$  ( $H_a$ ) is the out-of-plane (in-plane) anisotropy, and  $H_{\text{DM}}$  is the DM effective field. The exchange stiffness term consisting of  $H_{\text{ex}}$  and  $a_{\text{ex}}$  is discussed in the Supplemental Material, Table I [52], with a comparison between ferromagnetic (ferrimagnetic) [53] and antiferromagnetic models [54]. Coordinate axes are defined in the inset of Fig. 1(b). Considering a small

canting angle  $\theta$  induced by the DMI, the Cartesian coordinate defined with  $\mathbf{n}$  and  $\mathbf{m}$  at equilibrium is subsequently transformed to align with  $\mathbf{m}_1$  or  $\mathbf{m}_2$  in order to deduce the dynamics of the sublattices. By extracting the eigenfrequencies of Eq. (1), one derives the dispersion relations for both low-frequency and high-frequency AFM magnon modes (see the Supplemental Material, Sec. II [52]). Since only the low-frequency one is relevant for our experiments, we present its spin-wave dispersion here as

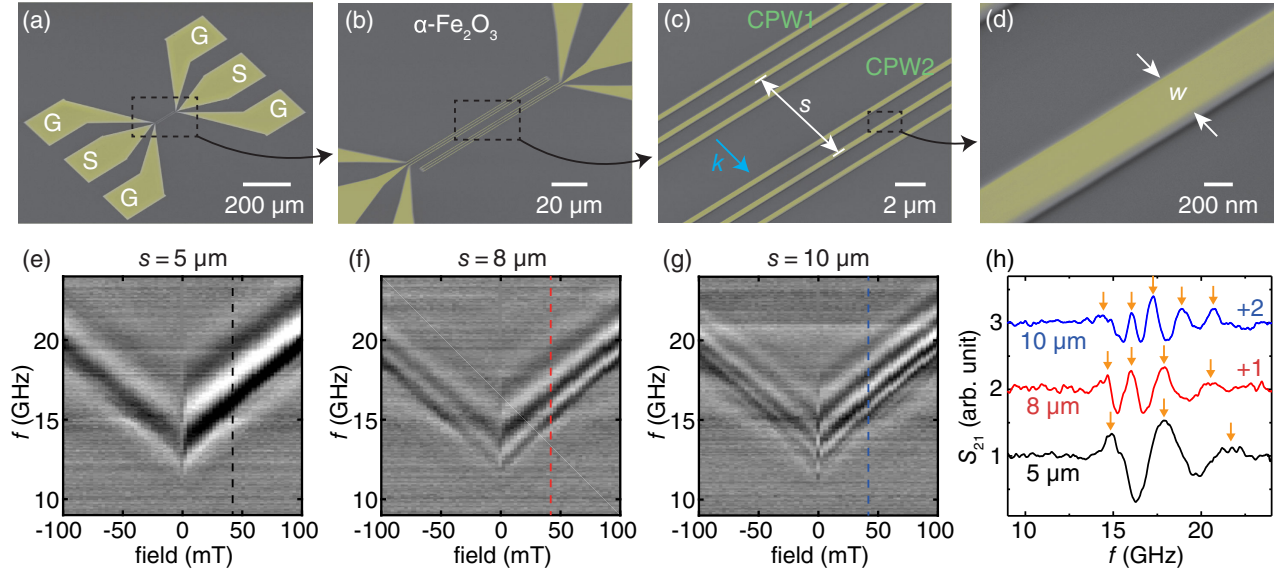


FIG. 2. (a) A global SEM image of two CPW antennas integrated on  $\alpha\text{-Fe}_2\text{O}_3$  with a GSG design. The pitch of the contact pad is  $250\ \mu\text{m}$ , compatible with microwave probes. The gray background represents  $\alpha\text{-Fe}_2\text{O}_3$  substrate. (b) SEM image within the black dashed square area in (a). (c) SEM-resolved image of a CPW. The center-to-center distance  $s$  between CPW1 and CPW2 for this device is  $8\ \mu\text{m}$ . The blue arrow indicates the spin-wave wave vector  $k$ . The yellow-rendered parts are the gold conducting lines whose width  $w = 380\ \text{nm}$  is characterized by the further close-up image in (d). (e)–(g) Spin-wave transmission spectra  $S_{12}$  measured by a vector network analyzer (imaginary part of the  $S$  parameter) and plotted as a function of applied magnetic field for three devices with different propagation distances  $s = 5, 8, 10\ \mu\text{m}$ . (h) Lineplots extracted at  $45\ \text{mT}$  for propagation distances  $s$ . Spectra are shifted for clarity. Orange arrows highlight the peak positions.

$$f = \frac{\gamma\mu_0}{2\pi} \sqrt{H_0(H_0 + H_{\text{DM}}) + 2H_a H_{\text{ex}} + H_{\text{ex}}^2 a_{\text{ex}}^2 k^2}, \quad (2)$$

where  $\gamma$  is the gyromagnetic ratio and  $\mu_0$  is the vacuum permeability. If on the one hand we take  $k = 0$ , the last term underneath the square root vanishes, and thereby it reduces to the uniform AFMR of a canted antiferromagnet as studied by Boverter *et al.* [51]. If on the other hand we do not introduce the DMI in the system, the first term beneath the square root disappears, and hence Eq. (2) becomes essentially the same as the dispersion for an easy-plane AFM such as NiO as analyzed by Rezende *et al.* [54] in the absence of DMI. In Fig. 1(b), we plot the spin-wave dispersion for the low-frequency mode in  $\alpha\text{-Fe}_2\text{O}_3$  based on Eq. (2) with  $\mu_0 H_0 = 60\ \text{mT}$ . Here we take the exchange field  $\mu_0 H_{\text{ex}} = 1040\ \text{T}$  from Ref. [43]. By fitting the field-dependent AFMR in a flip-chip measurement ( $k = 0$ ; see the Supplemental Material, Fig. S7 [52]), we extract the effective DM field  $\mu_0 H_{\text{DM}} = 2.7\ \text{T}$  and  $\mu_0 H_a = 0.067\ \text{mT}$ . These values are close to those in Refs. [50,51] and are adapted in plotting the dispersion in Fig. 1(b). Thus, the calculated dispersion relation predicts a group velocity of up to  $26.5\ \text{km/s}$ .

In the following, we present an experimental demonstration of high-velocity propagation of spin waves in  $\alpha\text{-Fe}_2\text{O}_3$  with all-electrical excitation and detection. The DMI-induced small canted moment can couple with an external microwave field and therefore provides us an

opportunity to excite antiferromagnetic spin waves with conventional coplanar waveguide antennas (CPWs) [6,14–16,25] fabricated on hematite using e-beam lithography and evaporation. Figures 2(a)–2(d) show the scanning electron microscope (SEM) images of the measured device with a spin-wave propagation distance  $s = 8\ \mu\text{m}$ . CPWs with a ground-signal-ground (GSG) design are patterned on a  $0.5\ \text{mm}$ -thick  $\alpha\text{-Fe}_2\text{O}_3$  crystal with e-beam lithography and connected to a vector network analyzer (VNA) to excite and detect spin waves. The spin-wave wave vectors excited by the CPWs are along the  $[11\bar{2}0]$  crystal orientation within the (0001) easy plane, which is the film plane. All measured devices are patterned on the same single-crystal film. Transmission spectra  $S_{21}$  (excitation at CPW1 and detection at CPW2) are measured by a VNA as a function of magnetic field, sweeping from negative to positive values. Data are shown in Figs. 2(e)–2(g) for propagation distances ( $s$ ) of  $5\ \mu\text{m}$ ,  $8\ \mu\text{m}$ , and  $10\ \mu\text{m}$ . The asymmetric amplitude of transmission spectra at positive and negative fields may arise from chiral magnetic near field emission induced by the nanoscale microwave antennas [57,58] in combination with the unconventional time-reversal symmetry breaking of hematite, which has been recently classified as an emergent magnetic phase altermagnetism [59]. A tentative theoretical model is discussed in the Supplemental Material, Sec. II [52] taking into account the chiral precession of the canted moment. Very recently, similar spin-wave nonreciprocity has been reported in

association with a surface mode observed in hematite [60]. Single spectra extracted at 45 mT are plotted together for three different propagation distances in Fig. 2(h). The transmission signal amplitude decays due to spin-wave damping. With increasing  $s$ , the observed signal oscillation becomes denser, and the number of peaks (marked by orange arrows) increases, for the following reason. The VNA is sensitive to the phase delay between both antennas, and the interval between two adjacent peaks corresponds to a phase difference  $\Delta\phi = 2\pi$ . Over a certain propagation distance  $s$ , the phase change is given by  $\Delta\phi = \Delta k \cdot s$ , where  $\Delta k$  represents a broad wave vector excitation generated by the nanoscale CPW antennas, as shown in Figs. 3(a) and 3(b). When  $\Delta\phi = \Delta k \cdot s$  reaches  $2\pi$ , the second peak appears, and the corresponding frequency interval  $\Delta f$  is observed [Fig. 3(d)]. Therefore, the spin-wave group velocity  $v_g$  can be estimated [14–16] using

$$v_g = \frac{\partial\omega}{\partial k} \approx \frac{2\pi\Delta f}{\Delta k} = \frac{2\pi\Delta f}{2\pi/s} = \Delta f \cdot s. \quad (3)$$

At different parts of the spin-wave dispersion in Fig. 3(c), the frequency intervals  $\Delta f$  differ ( $\Delta f_1 \neq \Delta f_2 \neq \Delta f_3$ ) in spite of an identical wave vector increment  $\Delta k = 2\pi/s$ .

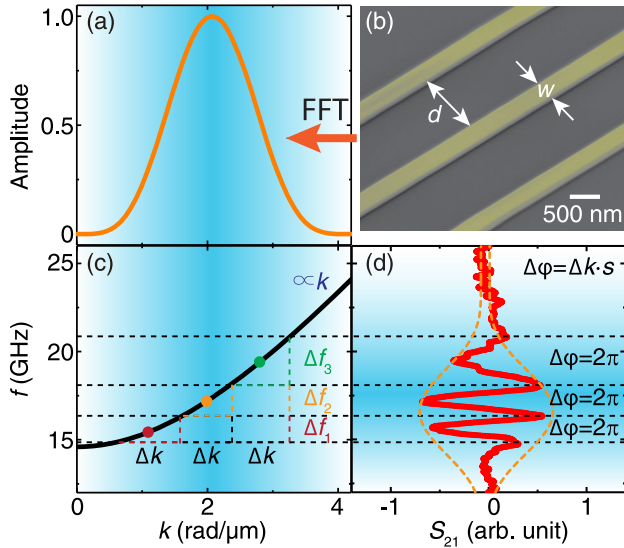


FIG. 3. (a) CPW-excited magnetic field wave vector distribution calculated by fast Fourier transformation (FFT) using the dimensions measured in the SEM image of (b) as  $w = 380$  nm and  $d = 1120$  nm. (c) AFM spin-wave dispersion plotted for 51 mT, where the background intensity represents the wave vector distribution imposed by CPW as shown in (a). Three equivalent wave vector segments  $\Delta k$  project into different frequency spans  $\Delta f_1$ ,  $\Delta f_2$ , and  $\Delta f_3$  in accordance with the dispersion. The frequency spans manifest themselves as peak-to-peak separation in the measured transmission spectrum  $S_{21}$  in (d). These frequency spans correspond to a phase change of  $2\pi$  after propagation over a certain distance  $s$ . The orange dashed curve in (d) defines an effective excitation envelope corresponding to the wave vector distribution of CPW in (a). Horizontal and vertical black dashed lines are a guide for the eyes.

The higher-frequency part of the dispersion presents a steeper slope,  $\Delta f_3 > \Delta f_2 > \Delta f_1$  as observed in Fig. 3(d). This indicates an increasing group velocity according to Eq. (3), given a fixed propagation distance  $s$ . Apart from the phase oscillation, the amplitude envelope (orange dashed arrows) is determined by the broad  $k$  excitation (blue shadow region) of the nanoscale CPW as characterized in Fig. 3(a). The frequency interval  $\Delta f_2$  located at the center of the envelope around 17.5 GHz therefore exhibits the largest oscillation amplitude. Based on Eq. (3), we can extract the average group velocity at about 17.5 GHz [orange dot in Fig. 3(c)] from a linear fitting of the measured frequency interval  $\Delta f$  as a function of  $1/s$ , as shown in the bottom-right inset of Fig. 4. The slope of the fitted red line yields a group velocity of about 14.2 km/s. Following this method, we extract group velocities at different frequency bands and plot them in Fig. 4 as the red open squares. The data acquisition from linear fittings of  $\Delta f$  versus  $1/s$  for frequencies of 15.9 GHz, 18.8 GHz, and 20.7 GHz are presented in the Supplemental Material, Sec. IV [52]. Two additional

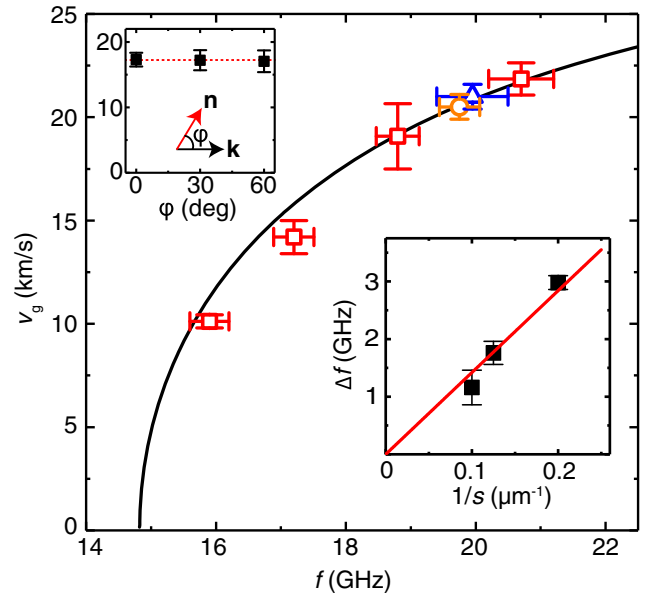


FIG. 4. AFM spin-wave group velocities for different frequencies extracted from the transmission spectra  $S_{21}$  at 51 mT. The values are given by the slope from a linear fit of  $\Delta f$  versus  $1/s$  based on Eq. (3). Bottom-right inset shows an example for the linear fitting of the measurement data around 17.2 GHz for three different propagation distances  $s = 5$   $\mu\text{m}$ ,  $8$   $\mu\text{m}$ , and  $10$   $\mu\text{m}$ . Red open squares are data obtained from the samples with the CPW design shown in Fig. 3(b). Orange circles and blue open triangles are data obtained from the samples with two other CPW designs with slightly different dimensions as described in the Supplemental Material, Sec. IV [52]. The solid line is the calculation taking the exchange length by fitting of our data  $a_{\text{ex}} = 1.7$   $\text{\AA}$ . Top-left inset presents the angle dependent group velocities at 51 mT and around 18.8 GHz. The red dotted line is a horizontal line around 18 km/s.

devices with slightly modified CPWs (Type 2 and Type 3) were also measured, and group velocities obtained from these two samples (see the Supplemental Material, Sec. IV [52]) are plotted as the orange circle and blue open triangle in Fig. 4. From the distance-dependent measurements, we extract a decay length of about 10  $\mu\text{m}$  for coherent AFM spin waves (see the Supplemental Material, Sec. V [52]). In conformity with the AFM spin-wave dispersion [Fig. 1(b)], we observe degenerate spin-wave modes (see the Supplemental Material, Sec. VI [52]) for different angles ( $\phi$ ) between the Néel vector ( $\mathbf{n}$ ) and wave vector ( $\mathbf{k}$ ), exhibiting almost identical spin-wave group velocities for different  $\phi$  (top-left inset of Fig. 4).

The group velocities extracted from different samples (Fig. 4) increase asymptotically toward a saturated group velocity (linear range in dispersion) of  $\gamma\mu_0 H_{\text{ex}} a_{\text{ex}}$ . The group velocity as a function of frequency can be derived from the dispersion [Eq. (2)]. By fitting our data, we obtain an exchange stiffness length  $a_{\text{ex}} = 1.7 \text{ \AA}$ , which could also be considered as an effective lattice constant in the 1D spin-chain model. This value corresponds to an AFM exchange stiffness [61] of about 10 pJ/m and a saturated velocity [62] of 30.2 km/s (see the Supplemental Material, Sec. II [52]). To approach the saturated velocity, we fabricate even smaller CPW antennas with larger wave vector  $k$  ( $\sim 5.2 \text{ rad}/\mu\text{m}$ ; see the Supplemental Material, Sec. VII [52]). With these CPWs, we did not observe clear signal oscillations in transmission spectra, which we attribute to the impedance mismatch due to the downscaling of the microwave antennas [63,64]. For micrometer-scale CPW antennas with small wave vectors ( $\sim 1.0 \text{ rad}/\mu\text{m}$ ; see the Supplemental Material, Sec. VII [52]), we again did not observe oscillating transmission signals owing to a low group velocity at the low- $k$  limit.

In summary, we experimentally observed the coherent propagating AFM spin waves at room temperature in a single-crystal  $\alpha\text{-Fe}_2\text{O}_3$ . Over a long distance of 10  $\mu\text{m}$ , the coherence of AFM spin waves can still be detected with a high group velocity of up to 22.5 km/s. With measurements using CPW antennas of different propagation distances, the AFM spin-wave dispersion could be indirectly characterized via the relationship between group velocities and frequencies. These data could be accounted for with a theoretical model that takes into account exchange, DM, Zeeman, and anisotropy energy. The AFM exchange stiffness length is estimated to be about 1.7  $\text{\AA}$ . One promising feature of AFM spin waves is their chirality, as it provides an additional degree of freedom. It has been shown that right- and left-handed modes can be detected electrically [39,65]. High-velocity coherent propagating AFM spin waves is suggestive of great prospects for coherent AFM magnonics.

The authors thank M. Elyasi, P. Gambardella, K. Yamamoto, and S. Maekawa for their helpful discussions. We wish to acknowledge the support by the National Key

Research and Development Program of China, Grants No. 2022YFA1402801 and No. 2022YFA1402603; NSF China under Grants No. 12074026, No. 52225106, No. 12241404, and No. U1801661; China Scholarship Council (CSC) under Grant No. 202206020091; and the Shenzhen Institute for Quantum Science and Engineering, Southern University of Science and Technology (Grant No. SIQSE202007).

*Note added.*—During the revision of this manuscript, we became aware that recent reports on spin-wave dispersion of hematite studied by Brillouin light scattering [66] and nonreciprocal propagation of spin waves in hematite [60] have been posted.

\*These authors contributed equally to this work.

†jean-philippe.ansermet@epfl.ch

‡songcheng@mail.tsinghua.edu.cn

§haiming.yu@buaa.edu.cn

- [1] V. Kruglyak, S. Demokritov, and D. Grundler, *Magnonics*, *J. Phys. D* **43**, 264001 (2010).
- [2] A. V. Chumak, V. I. Vasyuchka, A. A. Serga, and B. Hillebrands, *Magnon spintronics*, *Nat. Phys.* **11**, 453 (2015).
- [3] P. Pirro, V. I. Vasyuchka, A. A. Serga, and B. Hillebrands, *Advances in coherent magnonics*, *Nat. Rev. Mater.* **6**, 1114 (2021).
- [4] A. Barman *et al.*, *The 2021 magnonics roadmap*, *J. Phys. Condens. Matter* **33**, 413001 (2021).
- [5] L. J. Cornelissen, J. Liu, R. A. Duine, J. B. Youssef, and B. J. van Wees, *Long-distance transport of magnon spin information in a magnetic insulator at room temperature*, *Nat. Phys.* **11**, 1022 (2015).
- [6] C. Liu, J. Chen, T. Liu, F. Heimbach, H. Yu, Y. Xiao, J. Hu, M. Liu, H. Chang, T. Stueckler *et al.*, *Long-distance propagation of short-wavelength spin waves*, *Nat. Commun.* **9**, 738 (2018).
- [7] R. Lebrun, A. Ross, S. Bender, A. Qaiumzadeh, L. Baldrati, J. Cramer, A. Brataas, R. A. Duine, and M. Kläui, *Tunable long-distance spin transport in a crystalline antiferromagnetic iron oxide*, *Nature (London)* **561**, 222 (2018).
- [8] G. Csaba, A. Papp, and W. Porod, *Perspectives of using spin waves for computing and signal processing*, *Phys. Lett. A* **11**, 948 (2016).
- [9] A. V. Chumak *et al.*, *Advances in magnetism roadmap on spin-wave computing*, *IEEE Trans. Magn.* **58**, 0800172 (2022).
- [10] A. Serga, A. Chumak, and B. Hillebrands, *YIG magnonics*, *J. Phys. D* **43**, 264002 (2010).
- [11] H. Chang, P. Li, W. Zhang, T. Liu, A. Hoffmann, L. Deng, and M. Wu, *Nanometer-thick yttrium iron garnet films with extremely low damping*, *IEEE Magn. Lett.* **5**, 6700 (2014).
- [12] H. Qin, G. J. Both, S. J. Hämäläinen, L. Yao, and S. van Dijken, *Low-loss YIG-based magnonic crystals with large tunable bandgaps*, *Nat. Commun.* **9**, 5445 (2018).

- [13] Q. Wang *et al.*, Spin Pinning and Spin-Wave Dispersion in Nanoscopic Ferromagnetic Waveguides, *Phys. Rev. Lett.* **122**, 247202 (2019).
- [14] H. Yu, O. Allivy Kelly, V. Cros, R. Bernard, P. Bortolotti, A. Anane, F. Brandl, R. Huber, I. Stasinopoulos, and D. Grundler, Magnetic thin-film insulator with ultra-low spin wave damping for coherent nanomagnonics, *Sci. Rep.* **4**, 6848 (2014).
- [15] V. Vlaminck and M. Bailleul, Current-induced spin-wave Doppler shift, *Science* **322**, 410 (2008).
- [16] S. Neusser, G. Durr, H. G. Bauer, S. Tacchi, M. Madami, G. Woltersdorf, G. Gubbiotti, C. H. Back, and D. Grundler, Anisotropic Propagation and Damping of Spin Waves in a Nanopatterned Antidot Lattice, *Phys. Rev. Lett.* **105**, 067208 (2010).
- [17] A. Haldar, D. Kumar, and A. O. Adeyeye, A reconfigurable waveguide for energy-efficient transmission and local manipulation of information in a nanomagnetic device, *Nat. Nanotechnol.* **11**, 437 (2016).
- [18] K. Wagner, A. Kákay, K. Schultheiss, A. Henschke, T. Sebastian, and H. Schultheiss, Magnetic domain walls as reconfigurable spin-wave nanochannels, *Nat. Nanotechnol.* **11**, 432 (2016).
- [19] J. Han, P. Zhang, J. T. Hou, S. A. Siddiqui, and L. Liu, Mutual control of coherent spin waves and magnetic domain walls in a magnonic device, *Science* **366**, 1121 (2019).
- [20] M. Ishibashi, Y. Shiota, T. Li, S. Funada, T. Moriyama, and T. Ono, Switchable giant nonreciprocal frequency shift of propagating spin waves in synthetic antiferromagnets, *Sci. Adv.* **6**, eaaz6931 (2020).
- [21] Y. Liu, Z. Xu, L. Liu, K. Zhang, Y. Meng, Y. Sun, P. Gao, H.-W. Zhao, Q. Niu, and J. Li, Switching magnon chirality in artificial ferrimagnet, *Nat. Commun.* **13**, 1264 (2022).
- [22] K. Vogt, H. Schultheiss, S. Jain, J. E. Pearson, A. Hoffmann, S. D. Bader, and B. Hillebrands, Spin waves turning a corner, *Appl. Phys. Lett.* **101**, 042410 (2012).
- [23] B. Kalinikos and A. Slavin, Theory of dipole-exchange spin wave spectrum for ferromagnetic films with mixed exchange boundary conditions, *J. Phys. C* **19**, 7013 (1986).
- [24] V. Sluka *et al.*, Emission and propagation of 1D and 2D spin waves with nanoscale wavelengths in anisotropic spin textures, *Nat. Nanotechnol.* **14**, 328 (2019).
- [25] P. Che, K. Baumgaertl, A. Kúkolová, C. Dubs, and D. Grundler, Efficient wavelength conversion of exchange magnons below 100 nm by magnetic coplanar waveguides, *Nat. Commun.* **11**, 1445 (2020).
- [26] V. Baltz, A. Manchon, M. Tsoi, T. Moriyama, T. Ono, and Y. Tserkovnyak, Antiferromagnetic spintronics, *Rev. Mod. Phys.* **90**, 015005 (2018).
- [27] J. R. Hortensius, D. Afanasiev, M. Matthiesen, R. Leenders, R. Citro, A. V. Kimel, R. V. Mikhaylovskiy, B. A. Ivanov, and A. D. Caviglia, Coherent spin-wave transport in an antiferromagnet, *Nat. Phys.* **17**, 1001 (2021).
- [28] T. Jungwirth, X. Marti, P. Wadley, and J. Wunderlich, Antiferromagnetic spintronics, *Nat. Nanotechnol.* **11**, 231 (2016).
- [29] O. Gomonay, V. Baltz, A. Brataas, and Y. Tserkovnyak, Antiferromagnetic spin textures and dynamics, *Nat. Phys.* **14**, 213 (2018).
- [30] H. Qiu *et al.*, Manipulating Thz spin current dynamics by the Dzyaloshinskii-Moriya interaction in antiferromagnetic hematite, [arXiv:2209.10175](https://arxiv.org/abs/2209.10175).
- [31] T. Kampfrath, A. Sell, G. Klatt, A. Pashkin, S. Mährlein, T. Dekorsy, M. Wolf, M. Fiebig, A. Leitenstorfer, and R. Huber, Coherent terahertz control of antiferromagnetic spin waves, *Nat. Photonics* **5**, 31 (2011).
- [32] R. Lebrun, A. Ross, O. Gomonay, V. Baltz, U. Ebels, A.-L. Barra, A. Qaiumzadeh, A. Brataas, J. Sinova, and M. Kläui, Long-distance spin-transport across the Morin phase transition up to room temperature in ultra-low damping single crystals of the antiferromagnet  $\alpha$ -Fe<sub>2</sub>O<sub>3</sub>, *Nat. Commun.* **11**, 6332 (2020).
- [33] A. Ross, R. Lebrun, O. Gomonay, D. A. Grave, A. Kay, L. Baldrati, S. Becker, A. Qaiumzadeh, C. Ulloa, G. Jakob, F. Kronast, J. Sinova, R. Duine, A. Brataas, A. Rothschild, and M. Kläui, Propagation length of antiferromagnetic magnons governed by domain configurations, *Nano Lett.* **20**, 306 (2020).
- [34] J. Han, P. Zhang, Z. Bi, Y. Fan, T. S. Safi, J. Xiang, J. Finley, L. Fu, R. Cheng, and L. Liu, Birefringence-like spin transport via linearly polarized antiferromagnetic magnons, *Nat. Nanotechnol.* **15**, 563 (2020).
- [35] T. Wimmer, A. Kamra, J. Gückelhorn, M. Opel, S. Geprägs, R. Gross, H. Huebl, and M. Althammer, Observation of Antiferromagnetic Magnon Pseudospin Dynamics and the Hanle Effect, *Phys. Rev. Lett.* **125**, 247204 (2020).
- [36] S. Das, A. Ross, X. X. Ma, S. Becker, C. Schmitt, F. van Duijn, E. F. Galindez-Ruales, F. Fuhrmann, M.-A. Syskaki, U. Ebels, V. Baltz, A.-L. Barra, H. Y. Chen, G. Jakob, S. X. Cao, J. Sinova, O. Gomonay, R. Lebrun, and M. Kläui, Anisotropic long-range spin transport in canted antiferromagnetic orthoferrite YFeO<sub>3</sub>, *Nat. Commun.* **13**, 6140 (2022).
- [37] M. Dąbrowski, T. Nakano, D. M. Burn, A. Frisk, D. G. Newman, C. Klewe, Q. Li, M. Yang, P. Shafer, E. Arenholz, T. Hesjedal, G. van der Laan, Z. Q. Qiu, and R. J. Hicken, Coherent Transfer of Spin Angular Momentum by Evanescent Spin Waves Within Antiferromagnetic NiO, *Phys. Rev. Lett.* **124**, 217201 (2020).
- [38] C. Caspers, V. P. Gandhi, A. Magrez, E. de Rijk, and J.-Ph. Ansermet, Sub-terahertz spectroscopy of magnetic resonance in BiFeO<sub>3</sub> using a vector network analyzer, *Appl. Phys. Lett.* **108**, 241109 (2016).
- [39] J. Li *et al.*, Spin current from sub-terahertz-generated antiferromagnetic magnons, *Nature (London)* **578**, 70 (2020).
- [40] I. Boventer, H. Simensen, B. Brekke, M. Weides, A. Anane, M. Kläui, A. Brataas, and R. Lebrun, Antiferromagnetic Cavity Magnon Polaritons in Collinear and Canted Phases of Hematite, *Phys. Rev. Appl.* **19**, 014071 (2023).
- [41] S. Rezende, A. Azevedo, and R. L. Rodríguez-Suárez, Introduction to antiferromagnetic magnons, *J. Appl. Phys.* **126**, 151101 (2019).
- [42] F. J. Morin, Electrical properties of  $\alpha$ -Fe<sub>2</sub>O<sub>3</sub> containing titanium, *Phys. Rev.* **83**, 1005 (1951).
- [43] P. J. Besser, A. H. Morrish, and C. W. Searle, Magneto-crystalline anisotropy of pure and doped hematite, *Phys. Rev.* **153**, 632 (1967).

- [44] H. Jani, J.-C. Lin, J. Chen, J. Harrison, F. Maccherozzi, J. Schad, S. Prakash, C.-B. Eom, A. Ariando, T. Venkatesan, and P. G. Radaelli, Antiferromagnetic half-skyrmions and bimerons at room temperature, *Nature (London)* **590**, 74 (2021).
- [45] F. P. Chmiel *et al.*, Observation of magnetic vortex pairs at room temperature in a planar  $\alpha$ -Fe<sub>2</sub>O<sub>3</sub>/Co heterostructure, *Nat. Mater.* **17**, 581 (2018).
- [46] A. Wittmann *et al.*, Role of substrate clamping on anisotropy and domain structure in the canted antiferromagnet  $\alpha$ -Fe<sub>2</sub>O<sub>3</sub>, *Phys. Rev. B* **106**, 224419 (2022).
- [47] F. J. dos Santos, M. dos Santos Dias, and S. Lounis, Modeling spin waves in noncollinear antiferromagnets: Spin-flop states, spin spirals, skyrmions, and antiskyrmions, *Phys. Rev. B* **102**, 104436 (2020).
- [48] P. X. Zhang, C.-T. Chou, H. Yun, B. C. McGoldrick, J. T. Hou, K. A. Mkhoyan, and L. Liu, Control of Néel Vector with Spin-Orbit Torques in an Antiferromagnetic Insulator with Tilted Easy Plane, *Phys. Rev. Lett.* **129**, 017203 (2022).
- [49] M. Białek, J. Zhang, H. Yu, and J.-Ph. Ansermet, Antiferromagnetic resonance in  $\alpha$ -Fe<sub>2</sub>O<sub>3</sub> up to its Néel temperature, *Appl. Phys. Lett.* **121**, 032401 (2022).
- [50] H. Wang, Y. Xiao, M. Guo, E. Lee-Wong, G. Q. Yan, R. Cheng, and C. R. Du, Spin Pumping of an Easy-Plane Antiferromagnet Enhanced by Dzyaloshinskii-Moriya Interaction, *Phys. Rev. Lett.* **127**, 117202 (2021).
- [51] I. Boverter, H. T. Simensen, A. Anane, M. Kläui, A. Brataas, and R. Lebrun, Room-Temperature Antiferromagnetic Resonance and Inverse Spin-Hall Voltage in Canted Antiferromagnets, *Phys. Rev. Lett.* **126**, 187201 (2021).
- [52] See Supplemental Material at <http://link.aps.org/supplemental/10.1103/PhysRevLett.130.096701> for single-crystal  $\alpha$ -Fe<sub>2</sub>O<sub>3</sub> sample characterizations, spin-chain model for easy-plane antiferromagnetic spin waves with Dzyaloshinskii-Moriya interaction, magnetic parameters extracted from the field-dependent reflection spectra, different types of CPW antennas and their AFM spin-wave transmission spectra, group velocities extracted from experimental results, decay length estimated by experimental results, propagating AFM spin-wave transmission measurements at different angles between wavevector  $\mathbf{k}$  and Néel vector  $\mathbf{n}$ , spin-wave transmission spectra measured on the CPW antennas with higher and lower wavevectors, which includes Refs. [53,54].
- [53] E. H. Turner, Interaction of Phonons and Spin Waves in Yttrium Iron Garnet, *Phys. Rev. Lett.* **5**, 100 (1960).
- [54] S. M. Rezende, R. L. Rodríguez-Suárez, and A. Azevedo, Diffusive magnonic spin transport in antiferromagnetic insulators, *Phys. Rev. B* **93**, 054412 (2016).
- [55] J.-Ph. Ansermet and S. D. Brechet, *Principles of Thermodynamics* (Cambridge University Press, Cambridge, England, 2019).
- [56] R. M. Cornell and U. Schwertmann, *The Iron Oxides: Structure, Properties, Reactions, Occurrences, and Uses* (Wiley-VCH, Weinheim, 2003), Chap. 2.
- [57] T. Yu and G. E. W. Bauer, Noncontact Spin Pumping by Microwave Evanescent Fields, *Phys. Rev. Lett.* **124**, 236801 (2020).
- [58] V. E. Demidov, M. P. Kostylev, K. Rott, P. Krzysteczko, G. Reiss, and S. O. Demokritov, Excitation of microwaveguide modes by a stripe antenna, *Appl. Phys. Lett.* **95**, 112509 (2009).
- [59] L. Šmejkal, J. Sinova, and T. Jungwirth, Emerging Research Landscape of Altermagnetism, *Phys. Rev. X* **12**, 040501 (2022).
- [60] A. El Kanj, O. Gomonay, I. Boverter, P. Bortolotti, V. Cros, A. Anane, and R. Lebrun, Evidence of non-degenerated, non-reciprocal and ultra-fast spin-waves in the canted antiferromagnet  $\alpha$ -Fe<sub>2</sub>O<sub>3</sub>, [arXiv:2301.06329](https://arxiv.org/abs/2301.06329).
- [61] A. Scholl, M. Liberati, E. Arenholz, H. Ohldag, and J. Stöhr, Creation of an Antiferromagnetic Exchange Spring, *Phys. Rev. Lett.* **92**, 247201 (2004).
- [62] E. J. Samuelsen and G. Shirane, Inelastic neutron scattering investigation of spin waves and magnetic interactions in  $\alpha$ -Fe<sub>2</sub>O<sub>3</sub>, *Phys. Status Solidi* **42**, 241 (1970).
- [63] F. Ciubotaru, T. Devolder, M. Manfrini, C. Adelman, and I. Radu, All electrical propagating spin wave spectroscopy with broadband wavevector capability, *Appl. Phys. Lett.* **109**, 012403 (2016).
- [64] J. Lucassen, C. F. Schippers, L. Rutten, R. A. Duine, H. J. Swagten, B. Koopmans, and R. Lavrijsen, Optimizing propagating spin wave spectroscopy, *Appl. Phys. Lett.* **115**, 012403 (2019).
- [65] Y. Liu, H. Liu, W. Yuan, Y. Li, J. Li, Q. Shao, R. Cheng, and J. Shi, Controlling Antiferromagnetic Magnon Polarization by Interfacial Exchange Interaction, *Phys. Rev. Appl.* **18**, 034005 (2022).
- [66] M. Hamdi, F. Posva, and D. Grundler, Spin wave dispersion of ultra-low damping hematite ( $\alpha$ -Fe<sub>2</sub>O<sub>3</sub>) at GHz frequencies, [arXiv:2212.11887](https://arxiv.org/abs/2212.11887).